NANOSYSTEMS:
PHYSICS, CHEMISTRY, MATHEMATICS

Ali M., Elsaid M. *Nanosystems: Phys. Chem. Math.*, 2024, **15** (5), 658–669.
http://nanojournal.ifmo.ru
DOI 10.17586/2220-8054-2024-15-5-658-669

Original article

Effect of structural parameters, and spin-orbit interaction on the electronic properties of double quantum wire systems in the presence of external magnetic field

Mahmoud Ali, Mohammad Elsaid

Physics Department, An-Najah National University, Palestine

Corresponding author: Mohammad Elsaid, mkelsaid@najah.edu

ABSTRACT This study explores the effect of the structural parameters of the confining potential and external magnetic field on the electronic properties of a double quantum wire (DQW) system. Using theoretical analysis and graphical representations, we investigate the effects of varying parameters such as structural parameters (μ and λ) on the confinement potential profiles, probability density distributions and energy spectra of DQWs. Furthermore, we investigate the effect of variation of the confinement potential, the Rashba spin-orbit coupling and the external magnetic field on the energy spectra and the local density of states of the system. The changes in the energy spectra and the local density of states of the system due to Rashba spin-orbit coupling, and the external magnetic field were highlighted. The shifts and variations in energy and in the local density of states were discussed in detail. Our research results provide valuable insights into possibility of using the structural parameters and the external magnetic fields for control the electronic properties of the double quantum wire system.

KEYWORDS double quantum wire, spin-orbit interaction, local density of states

FOR CITATION Ali M., Elsaid M. Effect of structural parameters, and spin-orbit interaction on the electronic properties of double quantum wire systems in the presence of external magnetic field. *Nanosystems: Phys. Chem. Math.*, 2024, **15** (5), 658–669.

1. Introduction

The physical properties of semiconductors form the basis of the latest and current technological revolution, the development of ever smaller and more powerful devices, which affect not only the prospects of modern science but also practically all aspects of our daily life. This development is based on the ability to engineer the physical properties of semiconductors to make smaller devices with promising applications in high-performance devices [1–4]. Modern crystal growth techniques make it possible to grow layers of semiconductor material, which are so small that their physical properties are different from those of bulk materials. In these low-dimensional semiconductor structures, the carriers can be confined spatially, in quantum wires the electron is confined in two directions and can move freely only in the remaining direction. Quantum wires (QW) have been investigated widely and the number of published articles in this field increases because of their exciting applications, such as quantum wires laser, transistor, light-emitting diode, sensors, solar cells, optical filters, and displays [5–10]. Quantum wires have been made experimentally in different ways through various techniques, such as the vapor-liquid-solid (VLS) method, electron-beam lithography (EBL), nano sphere lithography, etching of quantum wells and ion implantation [11–15]. Two identical quasi-one-dimensional systems can be coupled by additional lateral confinement to produce a double quantum wire (DQW) structure. One-dimensional double quartic-well potential can be used to make double quantum wire heterostructures with controllable tunneling barrier thickness [16].

Both theoretical [17–23] and experimental studies [24, 25] have delved into the impact of the external magnetic field on the electronic and transport characteristics of the double quantum wire structure, formed by introducing a potential barrier that separates two identical narrow quantum wires. Huang and his research collaborators have examined the conductivity, thermoelectric power, and magnetization in ballistic coupled double quantum wires when exposed to an external magnetic field [26]. Additionally, Yenal Karaaslan et al. have investigated the conductivity and optical response of double quantum wires under the external magnetic and electric fields, considering Rashba and Dresselhaus spin-orbit couplings [27]. The change in the energy dispersion curve and ballistic conductance of a double quantum wire under the influence of the external magnetic field, electric field, and Rashba spin-orbit interaction are studied theoretically in [28]. The electronic transport properties of double QWs made of GaAs by considering impurity and external magnetic field were investigated by Korepov [29].

Sharma et al. have explored the influence of the temperature, hydrostatic pressure, and impurity on the energy spectrum, and ballistic conductivity of the $In_xGa_{1-x}As$ double QWR [30].

The investigation of the local density of states (LDOS) spectra has captivated the attention of numerous researchers, they have been motivated to explore the LDOS spectra due to their fundamental role in explaining the electronic structure and behavior of materials at the quantum level. By analyzing the LDOS, scientists gain valuable insights into the

distribution of electronic states within a given system, allowing for comprehension of its unique characteristics and functionalities. Consequently, researchers have conducted extensive investigations focusing on the comparison between LDOS results obtained through experimental work [31–33] and their associated theoretical counterparts [34–36]. Cristina Bena and Steven A. Kivelson calculated the local density of states in graphite theoretically in the presence of impurity [37]. The authors in reference [38] obtained the local density of states in graphene numerically by using the tight-binding model.

This paper is organized as follows: The Hamiltonian theory and computation procedures of double quantum wires are shown in the second section taking into consideration the Rashba spin-orbit coupling, the external magnetic field and the structural parameters. The computed results for eigenenergies, probability density, local density of states, and their dependence on the Rashba spin-orbit coupling, the external magnetic field and the structural parameters were presented in the third section. Section 4 is devoted to the conclusion.

2. Theory

The total Hamiltonian of an electron in the DQW which is subjected to an external magnetic field along the z-direction with Rashba spin-orbit coupling can be written as:

$$\hat{H} = \frac{(\vec{p} - e\vec{A})^2}{2m^*} + V_{\text{conf}}(x) + V_{\text{var}}(x) + H_R + H_{\text{Zeeman}}, \tag{1}$$

where $(\vec{p} - e\vec{A})$ is the canonical momentum, $\vec{p}$ is the momentum operator, $\vec{A}$ is the vector potential corresponding to the magnetic field along the z-direction, m^* is the effective mass of the electron in InSb-medium and e is the electron charge.

The double nanowires along the y-direction are characterized by a double-well confinement written as [39]:

$$V_{\text{conf}}(x) = \frac{1}{4}\lambda\left(x^2 - \frac{\mu^2}{\lambda}\right)^2, \tag{2}$$

where λ and μ are positive adjustable parameters for adjusting the width of the wires and the height of the barrier between the two-coupled wires, respectively [40]. The addition,

$$V_{\text{var}}(x) = V_0 \exp\left(-(x - x_1)^2/d^2\right), \tag{3}$$

has been taken as a variation of the confinement potential in the x-direction, where x_1 denotes the perturbation position and V_0 is the strength of the variation where d is a tunable parameter to impact variation stretch, this variation potential adds an extra potential to break the symmetry between the two wires in the double quantum wires (i.e a line of localized impurites at x_1 along the growth direction).

The Zeeman effect caused by the interaction between the electron spin and external magnetic field is given by:

$$\hat{H}_{\text{Zeeman}} = \frac{1}{2}g^*\mu_B B\sigma_z, \tag{4}$$

where g^* is the effective Lande g-factor, μ_B is the Bohr magneton and σ_z is the z-component of Pauli matrices.

The effects of Rashba spin-orbit coupling is taken into account by adding the following term [27]:

$$\hat{H}_R = \frac{\alpha_R}{h}\left[\sigma_x\left(p_y + eBx\right) - \sigma_y p_x\right]. \tag{5}$$

Here α_R is the Rashba spin-orbit coupling parameters, σ_x, σ_y are the x- and y-component of the Pauli matrices, and p_x, p_y are the components of the electron momentum.

The local density of states can give information about the tunneling current and the tunneling conductance in the STM spectroscopy:

$$LDOS(r, E) = \sum_{n=1}^{N} |\psi_n|^2 \delta(E - E_n). \tag{6}$$

The delta function that appears in the LDOS can be replaced by a more practical expression in the computational process [41]:

$$LDOS(E) = \frac{1}{\sqrt{2\pi\Gamma^2}} \sum_n |\psi_n|^2 \exp\left(-\frac{(E - E_n)^2}{2\Gamma^2}\right), \tag{7}$$

where Γ is the broadening factor and E_n is the energy value for the n-th eigenstate.

The continuous spectrum eigenfunctions of the Hamiltonian can be expressed in terms of plane waves due to the translational invariance along the y-direction as:

$$\psi(x,\ y) = \varphi(x)\exp(ik_y y), \tag{8}$$

where k_y represents the wave numbers of the plane wave along the y-direction. The Schrödinger equation becomes separable in x and y and, accordingly, the Hamiltonian ($H = H_1 + H_2 + H_R + V_{\text{imp}}$) can be rewritten as follows:

$$H_1 = \left[-\frac{h^2}{2m^*}\frac{d^2}{dx^2} + \frac{1}{2}m^*\omega^2(x - x_0)^2 + \frac{\omega_0^2}{\omega^2}\frac{h^2k_y^2}{2m^*} \right] \sigma_0 \; + \frac{1}{2}g^*\mu_B B\sigma_z, \tag{9}$$

$$H_2 = \left[-\frac{1}{2}\left(m^*\omega_0^2 + \mu^2\right)x^2 + \frac{1}{4}\lambda x^4 + \frac{1}{4}\frac{\mu^4}{\lambda} \right] \sigma_0, \tag{10}$$

$$H_R = \alpha_R \left[\sigma_x \left(k_y + \frac{eB}{h}x \right) + i\sigma_y \frac{d}{dx} \right], \tag{11}$$

$$V_{\text{var}}(x) = V_0 \exp\left[-\frac{(x - x_1)^2}{d^2} \right]. \tag{12}$$

Here ω_0 is the harmonic oscillator frequency, $\omega = \sqrt{\omega_0^2 + \omega_c^2}$ is the effective oscillator frequency and $\omega_c = eB/m^*$ is the cyclotron frequency, $l_0 = \sqrt{\hbar/m^*\omega_0}$ is the characteristic length of the harmonic oscillator and $x_0 = -\dfrac{l_0^2\widetilde{\omega}_c k_y}{\widetilde{\omega}_c^2 + 1}$ is the guiding center coordinate where $\widetilde{\omega}_c = \dfrac{\omega_c}{\omega_0}$ and $\widetilde{\omega} = \dfrac{\omega}{\omega_0} = \sqrt{\widetilde{\omega}_c^2 + 1}$.

The set of eigenfunctions of H_1 is given as:

$$\phi_{n\sigma}(x) = \frac{1}{\sqrt{l_0\sqrt{\frac{\pi}{\sqrt{\widetilde{\omega}_c^2+1}}}2^n n!}} H_n\left(\frac{x - x_0}{\frac{l_0}{\sqrt[4]{\widetilde{\omega}_c^2+1}}} \right) \exp\left(-\frac{1}{2}\left(\frac{x - x_0}{\frac{l_0}{\sqrt[4]{\widetilde{\omega}_c^2+1}}} \right)^2 \right) \chi_\sigma. \tag{13}$$

Here $H_n(x)$ are the Hermite polynomials of integer order n, χ_σ are the spinor functions with $\chi_+ = \begin{pmatrix} 1 \\ 0 \end{pmatrix}$ for spin-up and $\chi_- = \begin{pmatrix} 0 \\ 1 \end{pmatrix}$ for spin-down in the z-direction.

By using the set of eigenfunctions of H_1, the matrix elements of the full Hamiltonian can be written as:

$$\langle \phi_{n\sigma} | H | \phi_{m\sigma'} \rangle = \langle \phi_{n\sigma} | H_1 | \phi_{m\sigma'} \rangle + \langle \phi_{n\sigma} | H_2 | \phi_{m\sigma'} \rangle + \langle \phi_{n\sigma} | H_R | \phi_{m\sigma'} \rangle + \langle \phi_{n\sigma} | V_{\text{var}} | \phi_{m\sigma'} \rangle . \tag{14}$$

The energy eigenvalues corresponding to H_1 are as follows:

$$\frac{E_1}{\hbar\omega_0} = \sqrt{\widetilde{\omega}_c^2 + 1}\left(n + \frac{1}{2} \right) + \frac{l_0^2 k_y^2}{2(\widetilde{\omega}_c^2 + 1)} \pm \frac{g^*\mu_B B}{2\hbar\omega_0} \tag{15}$$

and the matrix elements corresponding to H_2 are:

$$\left\langle \phi_{n\sigma} \left| \frac{H_2}{\hbar\omega_0} \right| \phi_{m\sigma'} \right\rangle = A_{-4}\delta_{n,m-4} + A_{-3}\delta_{n,m-3} + A_{-2}\delta_{n,m-2} + A_{-1}\delta_{n,m-1} + A_0\delta_{n,m} + A_{+1}\delta_{n,m+1} + A_{+2}\delta_{n,m+2} + A_{+3}\delta_{n,m+3} + A_{+4}\delta_{n,m+4}, \tag{16}$$

where:

$$A_{-4}=\frac{1}{16}\frac{\widetilde{\lambda}}{\widetilde{\omega}_c^2+1}\sqrt{(n+4)(n+3)(n+2)(n+1)},$$

$$A_{-3}=\frac{1}{4}\frac{x_0}{l_0\sqrt{\widetilde{\omega}_c^2+1}}\widetilde{\lambda}\sqrt{\frac{2}{\sqrt{\widetilde{\omega}_c^2+1}}(n+3)(n+2)(n+1)},$$

$$A_{-2}=\frac{1}{4\sqrt{\widetilde{\omega}_c^2+1}}\sqrt{(n+2)(n+1)}\left[\widetilde{\lambda}\left(3\frac{x_0^2}{l_0^2}+\frac{1}{\sqrt{\widetilde{\omega}_c^2+1}}\left(n+\frac{3}{2}\right)\right)-\left(1+\widetilde{\mu}^2\right)\right],$$

$$A_{-1}=\frac{1}{2}\frac{x_0}{l_0}\sqrt{\frac{2}{\sqrt{\widetilde{\omega}_c^2+1}}(n+1)}\left[\widetilde{\lambda}\left(\frac{x_0^2}{l_0^2}+\frac{3}{2\sqrt{\widetilde{\omega}_c^2+1}}(n+1)\right)-\left(1+\widetilde{\mu}^2\right)\right],$$

$$A_0=\frac{1}{4}\widetilde{\lambda}\left[\frac{x_0^4}{l_0^4}+\frac{3}{\sqrt{\widetilde{\omega}_c^2+1}}\frac{x_0^2}{l_0^2}(2n+1)+\frac{\widetilde{\mu}^4}{\widetilde{\lambda}^2}\right]+\frac{1}{4}\widetilde{\lambda}\left[\frac{3}{2\left(\widetilde{\omega}_c^2+1\right)}\left(n^2+n+\frac{1}{2}\right)\right]-$$
$$\frac{1}{2}\left(1+\widetilde{\mu}^2\right)\left[\frac{x_0^2}{l_0^2}+\frac{1}{\sqrt{\widetilde{\omega}_c^2+1}}\left(n+\frac{1}{2}\right)\right],$$

$$A_{+1}=\frac{1}{2}\frac{x_0}{l_0}\sqrt{\frac{2}{\sqrt{\widetilde{\omega}_c^2+1}}n}\left[\widetilde{\lambda}\left(\frac{x_0^2}{l_0^2}+\frac{3}{2\sqrt{\widetilde{\omega}_c^2+1}}n\right)-\left(1+\widetilde{\mu}^2\right)\right],$$

$$A_{+2}=\frac{1}{4\sqrt{\widetilde{\omega}_c^2+1}}\sqrt{n(n-1)}\left[\widetilde{\lambda}\left(3\frac{x_0^2}{l_0^2}+\frac{1}{\sqrt{\widetilde{\omega}_c^2+1}}\left(n-\frac{1}{2}\right)\right)-\left(1+\widetilde{\mu}^2\right)\right],$$

$$A_{+3}=\frac{1}{4}\widetilde{\lambda}\frac{x_0}{l_0\sqrt{\widetilde{\omega}_c^2+1}}\sqrt{\frac{2}{\sqrt{\widetilde{\omega}_c^2+1}}n(n-1)(n-2)},$$

$$A_{+4}=\frac{1}{16(\widetilde{\omega}_c^2+1)}\widetilde{\lambda}\sqrt{n(n-1)(n-2)(n-3)},$$

with $\widetilde{\lambda}=\dfrac{\lambda\hbar\omega_0}{\left(m^*\omega_0^2\right)^2}$ and $\widetilde{\mu}=\dfrac{\mu}{\sqrt{m^*}\omega_0}$.

The matrix elements of Rashba Hamiltonian H_R are given by the expression:

$$\left\langle\phi_{n\sigma}\left|\frac{H_R}{\hbar\omega_0}\right|\phi_{m\sigma'}\right\rangle=\sqrt{2\frac{\Delta_R}{\hbar\omega_0}}\left[l_0k_y\left(1-\frac{\widetilde{\omega}_c^2}{\widetilde{\omega}_c^2+1}\right)\right]\delta_{n,m}+$$
$$\sqrt{2\frac{\Delta_R}{\hbar\omega_0}\sqrt{\widetilde{\omega}_c^2+1}}\left[\left(\frac{\widetilde{\omega}_c}{\sqrt{\widetilde{\omega}_c^2+1}}\pm1\right)\sqrt{\frac{(n+1)}{2}}\delta_{n,m-1}+\left(\frac{\widetilde{\omega}_c}{\sqrt{\widetilde{\omega}_c^2+1}}\mp1\right)\sqrt{\frac{n}{2}}\delta_{n,m+1}\right], \quad (17)$$

where: $\Delta_R=\dfrac{\alpha_R^2m^*}{2\hbar^2}$.

The matrix elements of the variation Hamiltonian are presented by the expression:

$$\left\langle\phi_{n\sigma}\left|\frac{V_{\text{var}}(x)}{\hbar\omega_0}\right|\phi_{m\sigma'}\right\rangle=\left\langle\phi_{n\sigma}\left|\frac{V_0}{\hbar\omega_0}\exp\left(-\frac{(x-x_1)^2}{d^2}\right)\right|\phi_{m\sigma'}\right\rangle, \quad (18)$$

which can be simplified by using the standard integral [42]:

$$\int_{-\infty}^{\infty}\mathrm{e}^{-(x-y)^2}H_m(\alpha x)H_n(\alpha x)\,dx=\pi^{1/2}\sum_{k=0}^{\min(m,n)}2^kk!\binom{m}{k}\binom{n}{k}\left(1-\alpha^2\right)^{\frac{m+n}{2}-k}H_{m+n-2k}\left[\frac{\alpha y}{\left(1-\alpha^2\right)^{1/2}}\right]. \quad (19)$$

The matrix elements of $V_{\text{var}}(x)$ can be written as:

$$\left\langle\phi_{n\sigma}\left|\frac{V_{\text{var}}(x)}{\hbar\omega_0}\right|\phi_{m\sigma'}\right\rangle=\frac{V_0}{\sqrt{2^{n+m}n!m!}}\times\sqrt{\frac{\sqrt{\widetilde{\omega}_c^2+1}}{\sqrt{\widetilde{\omega}_c^2+1}+\frac{1}{d^2}}\exp\left[\frac{-\left(x_0-x_1\right)^2\left(1-\frac{1}{d^2}\right)}{\frac{\sqrt{\widetilde{\omega}_c^2+1}}{\sqrt{\widetilde{\omega}_c^2+1}+\frac{1}{d^2}}d^2}\right]}\times$$
$$\sum_{k=0}^{\min(m,n)}2^kk!\binom{m}{k}\binom{n}{k}\times\left(\frac{\sqrt{\widetilde{\omega}_c^2+1}}{\sqrt{\widetilde{\omega}_c^2+1}+\frac{1}{d^2}}\right)^{\frac{m+n}{2}-k}H_{m+n-2k}\left[\frac{\frac{-(x_0-x_1)}{d^2}\sqrt[4]{\widetilde{\omega}_c^2+1}/(\sqrt{\widetilde{\omega}_c^2+1}+\frac{1}{d^2})}{\sqrt{\left(1-\sqrt{\widetilde{\omega}_c^2+1}\right)/\sqrt{\widetilde{\omega}_c^2+1}+\frac{1}{d^2}}}\right]. \quad (20)$$

In the calculations the characteristic length l_0 corresponding to the confinement potential is chosen as the length scale and, consequently, the energy scale becomes to be $\hbar\omega_0$. The parameters used in the numerical calculations are the effective mass of Indium Antimonide (InSb) ($m^* = 0.015m_e$) and the effective Lande-g factor ($g^* = 51$) [43].

The changes in the confinement potential shape, influenced by structural parameters and varying across the x-coordinates, are illustrated in Fig. 1, while keeping the parameter $\widetilde{\lambda}$ constant. In Fig. 1(a), it is evident that for $\widetilde{\mu} = 0$, the confinement exhibits a SQW (single quantum wire) structure. However, for $\widetilde{\mu} \neq 0$, the potential confines the carriers within two narrower wires, resulting in a DQW (double quantum wire) confinement. To investigate the influence of the adjustable parameter μ, the confinement potential has been graphically represented for various $\widetilde{\mu}$ values in Fig. 1(b). As μ increases, the barrier between the two wires becomes higher. Consequently, the probability of carriers tunneling between the wires decreases. Therefore, the increase in $\widetilde{\mu}$ acts as a controlling factor, influencing the confinement potential and, in turn, limiting the probability of quantum tunneling events between the two distinct wires.

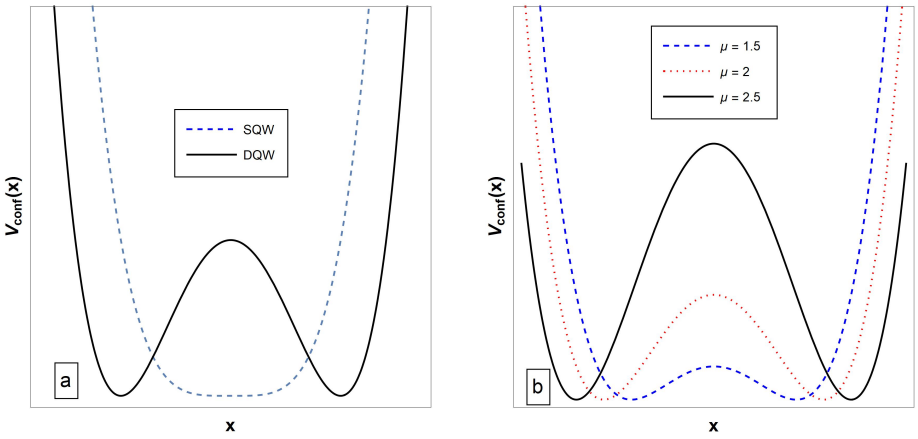

FIG. 1. Confinement potential profile versus the growth direction coordinate a) SQW and DQW; b) DQW for different $\widetilde{\mu}$ at fixed $\widetilde{\lambda}$ value

In Fig. 2, the influence of the adjustable parameter $\widetilde{\mu}$ on probability density is apparent. When $\widetilde{\mu}$ is set to zero, As illustrated in Fig. 2(a), choosing $\widetilde{\mu} = 0$ leads to the formation of a single quantum wire (SQW) shape. Fig. 2(a) presents a clear representation of the probability density distribution for the first few energy levels. However, in Figs. 2(b) ($\widetilde{\mu} = 2$) and 2(c) ($\widetilde{\mu} = 2.5$), the introduction of a barrier results in a double quantum wires (DQW) configuration, causing a noticeable change in the distribution of the probability density. The effect of the barrier on the probability density is evident, as it decreases the probability density in its location of effect, especially for states with initially higher probability density at the barrier position. The redistributed probability density is equally distributed in two wires, and the energy value for each state increases. This increase is greater for the levels that had a higher probability at the location of the barrier's effect. For example, the barrier's impact on the first level is greater than its impact on the second level because the wave function for the first level has an antinode at the barrier's location. Consequently, the barrier divides the probability into two equal parts in each wire, and the energy increase for this level is significant. As for the second level, it originally had a node in its wave function in the barrier's location, which resulted in a smaller energy increase compared to the first level. Therefore, the first and second levels become degenerate within each wire. Furthermore, as $\widetilde{\mu}$ increases, the barrier height also increases, affecting higher energy states. Therefore, $\widetilde{\mu}$ causes a degenerate state in each wire and also causes symmetry degeneracy in probability density across the two wires, as it is clear from the comparison between Figs. 2(a and b). The symmetry degeneracy becomes more pronounced at higher energy levels as the value of $\widetilde{\mu}$ increases, as illustrated in Fig. 2(c).

Figure 2.

Figure 3 provides insight into the effect of potential variation on the probability density within a double quantum wire system. The variation was placed in the center of one of the wires ($x_1/l_0 = 1.2$) as shown in Fig. 3(a), the variation in the confinement potential significantly influenced the probability density of the energy levels. A comparative analysis between Fig. 3(a) and Fig. 3(b) reveals a significant change in the probability density due to variation in the potential which results in the elevation of the energy levels within the wire where they are situated ($V_0 \exp(-(x - x_0)^2/d^2)$) where d (which represents the standard deviation of the Gaussian function) is chosen to be small ($d/l_0 = 0.5$) to get more localized potential. This effect leads to large redistribution of the probability density resulting in the elimination of the symmetry degeneracy which is clearly evident in the Fig. 3(a). From the comparison, it becomes evident that the probability density has undergone a marked redistribution. For example, the first peak in the left wire now corresponds to the ground energy level, while the first peak in the right wire represents the first exited energy level. So the energy levels have been extensively redistributed, and the symmetry degeneracy has been removed.

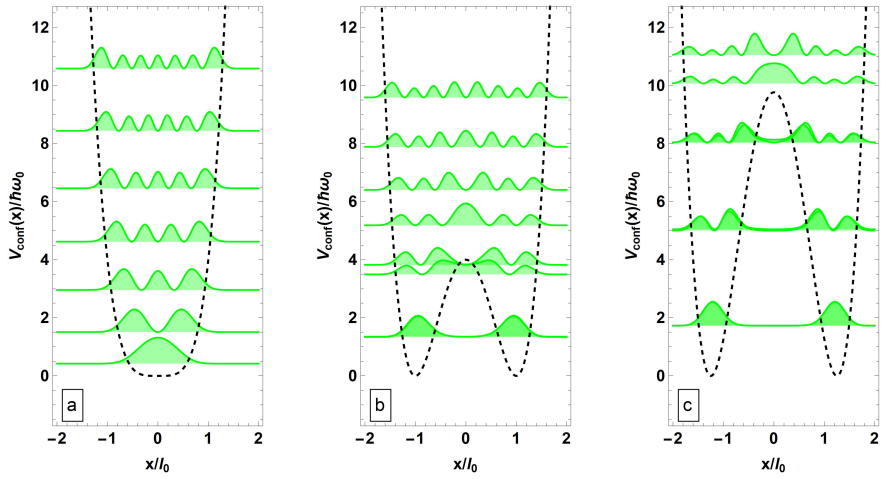

FIG. 2. The confinement potential and square wave functions corresponding to the first few energy levels: a) for SQW; b) DQW at $\widetilde{\mu} = 2$ and $\widetilde{\lambda} = 1$; c) DQW at $\mu = 2.5$ and $\widetilde{\lambda} = 1$

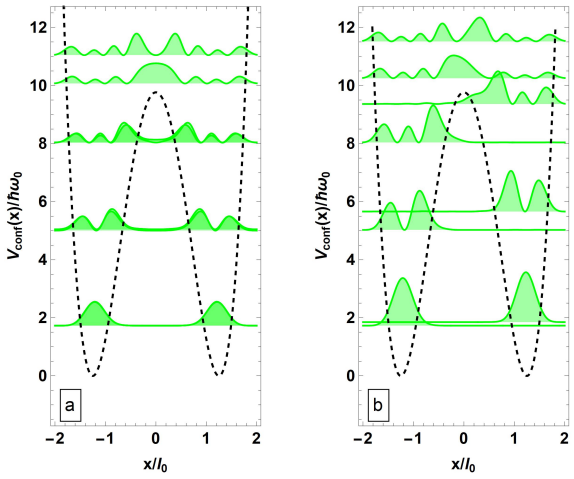

FIG. 3. The confinement potential and square wave functions corresponding to the first few energy levels: a) DQW at $\widetilde{\mu} = 2.5$ and $\widetilde{\lambda} = 1$ without variation; b) DQW at $\widetilde{\mu} = 2.5$ and $\widetilde{\lambda} = 1$, $V_0/(\hbar\omega_0) = 3$, $x_1/l_0 = 1.2$ and $d/l_0 = 0.5$

The influence of the parameter $\widetilde{\mu}$ on merging energy levels is distinctly evident in Fig. 4(a). It is apparent that at higher values of $\widetilde{\mu}$, the merging is exhibiting at higher energy levels. Additionally, the energy levels associated with the system have a degeneracy related to the spin of the electron, namely, each line in the figure represents two degenerate energy levels due to the spin of the electron. The external magnetic field has a significant effect, as shown in Fig. 4(b). The external magnetic field plays a dual role by removing the spin degeneracy and causing the separation of energy levels that were previously merged due to the confinement potential in each wire. This leads to a noticeable change in the levels of the energy and provides a clear illustration of the magnetic field's influence on the quantum characteristics of the system. The external magnetic field results in a shift up in the energy levels of the system. This shift is dependent on the magnetic field strength, and each energy level in the system will split into two sublevels due to the interaction with the external magnetic field, i.e. this leads to the remove of the degeneracy in the energy levels. In conclusion, the external magnetic field has an essential effect on the double quantum wire system, causing the splitting of energy levels and giving rise to changes in the electronic structure. The ability to adjust the strength of the external magnetic field provides a technique to organize energy levels and control the electronic properties of the double quantum wire system.

For a more focused analysis of the magnetic field and Rashba spin-orbit coupling effect on the DQW system, Fig. 5 has been introduced. Fig. 5(a) illustrates the effect of the magnetic field on certain energy levels within the system. It is observed in the figure that the energy levels are merged due to the influence of the barrier potential created by the confinement potential. Lower energy levels experience a more significant impact from the barrier since they are situated where its effect is stronger. In the higher energy levels, the influence of the barrier diminishes. Thus, in lower energy

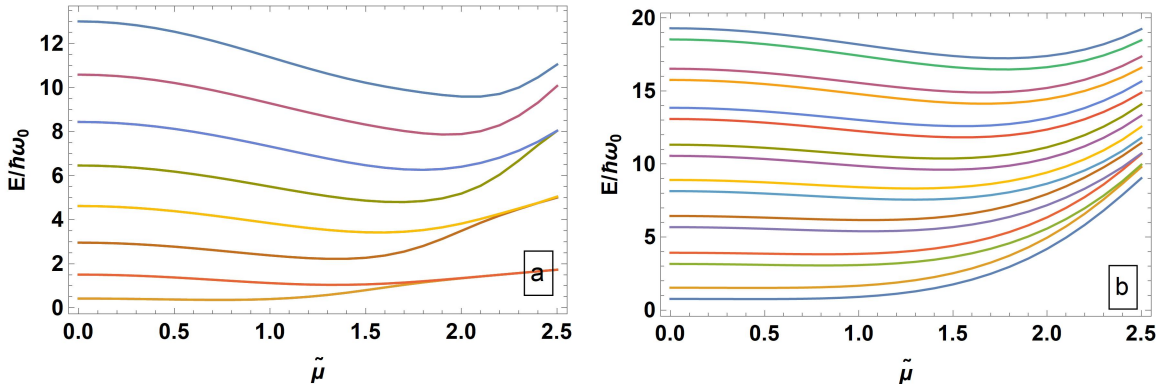

FIG. 4. The energy versus $\widetilde{\mu}$: a) at $\widetilde{\omega}_c = 0$; b) at $\widetilde{\omega}_c = 2$, at $\widetilde{\lambda} = 1$

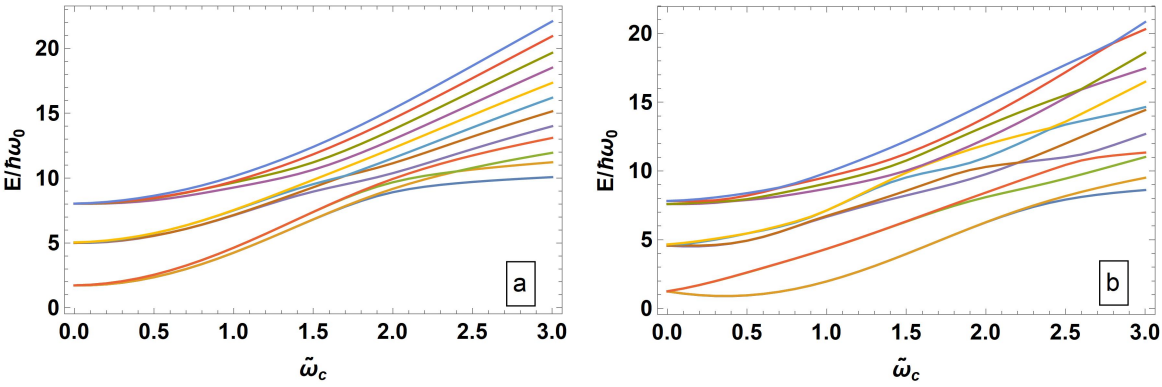

FIG. 5. The energy dispersion at $k_y l_0 = 0$ as a function of $\widetilde{\omega}_c$ for $\widetilde{\mu} = 2.5$, $\widetilde{\lambda} = 1$; a) $\Delta_R/(\hbar\omega_0) = 0$; b) $\Delta_R/(\hbar\omega_0) = 0.5$

levels where the influence of the barrier is significant, the magnetic field needs more strength to separate the merged energy levels, while higher energy levels require a smaller magnetic field strength. As illustrated in the figure, the magnetic field eliminates the spin degeneracy and separates the merged energy levels, raising the energy for all levels. This emphasizes the role of the magnetic field in redistributing and controlling the energy levels, thereby influencing and controlling the physical properties of the DQW system.

The interaction between the magnetic field and the Rashba spin-orbit coupling plays a crucial role in creating a significant separation in spin-up and spin-down branches of the energy levels. When higher magnetic field values are applied, the behavior of the energy spectrum becomes complicated compared to the case where no Rashba spin-orbit coupling is present. The interaction between the magnetic field and the Rashba spin-orbit coupling results in anti-crossings between the various sub-bands of the energy states leading to a more complex and rich structure in the overall energy spectrum of the system. These anti-crossings represent points where the energy levels of different spin states intersect, providing a unique insight into the dynamics of the system under the influence of both magnetic field and Rashba spin-orbit coupling as demonstrated in Fig. 5(b).

Figure 6 illustrates the effect of the variation positions and strength, as well as the external magnetic field on the energy levels in two cases: when $\widetilde{\mu} = 0$ (no barrier, SQW) and when $\widetilde{\mu} = 2.5$ (barrier, DQW). Through a detailed examination of Fig. 6(a and b) which represents the first case, the effect of the variation on the energy levels at each position in the SQW system becomes evident. This effect occurs at the positions where there is a probability density of the energy level. Consequently, the extra potential will raise the energy levels at these positions. This also clarifies the probability density distribution in this case which we have previously discussed in Fig. 2. The magnetic field eliminates the spin degeneracy. It separates the spin-up and spin-down branches of the energy levels. In Figure 6 (c and d), the effect of the variation's position and the external magnetic field for the second case ($\widetilde{\mu} = 2.5$) is explained. Initially, the presence of the barrier re-distributes the energy levels, resulting in the merging of the first level with the second and the third level with the fourth. This phenomenon was previously illustrated in the second figure. Consequently, each spectral line corresponding to the energy levels represents a combination of four distinct levels: two merged due to the barrier and two merged due to spin degeneracy. The introduction of asymmetric variation separates the merged levels caused by the barrier. Additionally, the application of an external magnetic field breaks the degeneracy associated with the spins.

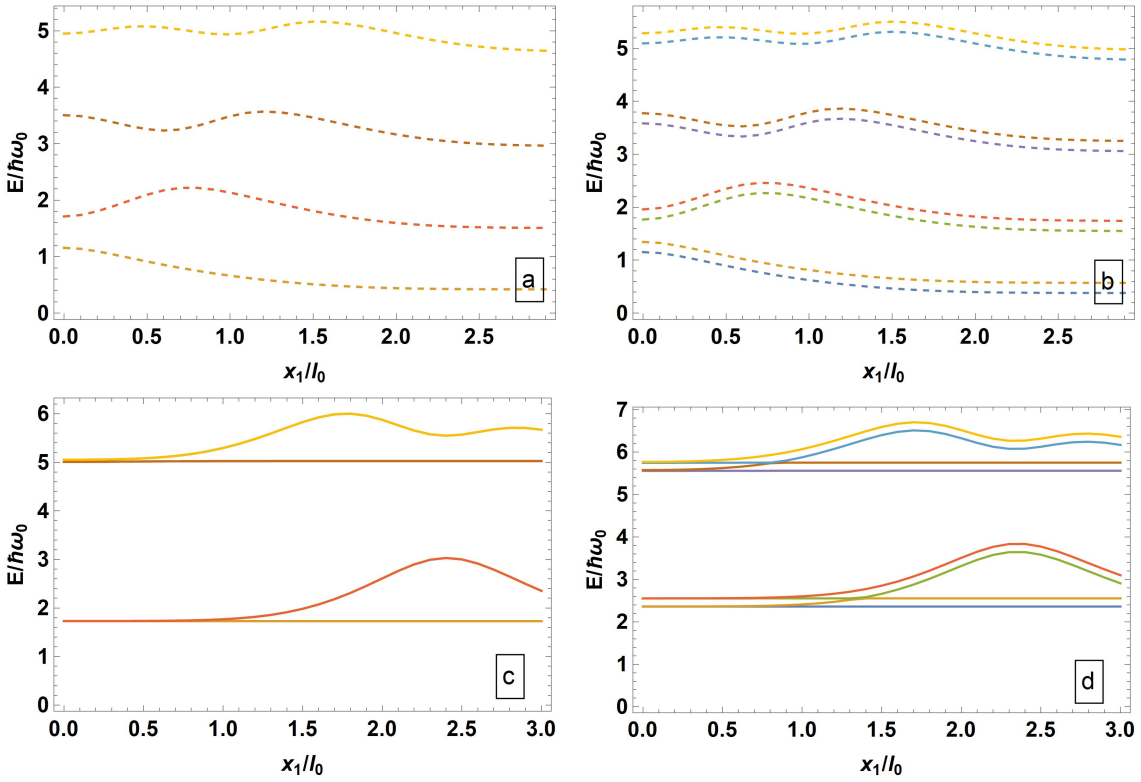

FIG. 6. The energy dispersion at $k_y l_0 = 0$ versus x_1/l_0 for $(V_0/(\hbar\omega_0) = 5$, $d/l_0 = 0.5$; a) $\widetilde{\mu} = 0$, $\widetilde{\lambda} = 1, \widetilde{\omega}_c = 0$; b) $\widetilde{\mu} = 0, \widetilde{\lambda} = 1, \widetilde{\omega}_c = 0.5$; c) $\widetilde{\mu} = 2.5, \widetilde{\lambda} = 1, \widetilde{\omega}_c = 0$; d) $\widetilde{\mu} = 2.5, \widetilde{\lambda} = 1, \widetilde{\omega}_c = 0.5$

In Fig. 7, the local density of states has been plotted at $(x/l_0 = 0)$ as a function of energy for $(\widetilde{\mu}= 0)$ dashed line and for $(\widetilde{\mu}= 2.5)$ solid line at a fixed value of$\widetilde{\lambda}$ $(\widetilde{\lambda}= 1)$. The vertical lines in the LDOS figure reflect the quantized nature of the energy levels and the presence of localized quantum states, and it gives one an idea about the spatial distribution of electronic wavefunctions in the confined system. These features offer valuable insights into the electronic properties of the quantum system at a local scale. The vertical dashed lines in Fig. 7 result from specific energy levels at $(x/l_0 = 0)$ position for a single quantum wire $(\widetilde{\mu} = 0)$, these lines represent energy levels with probability density at the center of the wire. This is evident when referring back to Fig. 2, where these vertical dashed lines in the figure correspond to the odd-numbered energy levels, such as the first and the third levels. These levels exhibit peaks in probability density at the center of the wire. The solid line represents the local density of states at $(x/l_0 = 0)$ position for a double quantum wire separated by a barrier $(\widetilde{\mu} = 2.5)$ (see Fig. 2). The presence of the barrier rearranges the probability density distribution as shown in Fig. 2. It is clear that the lowest energy levels, are significantly affected by the barrier and they lose the probability density at $(x/l_0 = 0)$ position compared with $(\widetilde{\mu} = 0)$ case. Consequently, the local density of states at $(x/l_0 = 0)$ position will not have vertical lines for these lower energy levels. On the other hand, higher energy levels that are not significantly affected by the barrier exhibit vertical lines in the local density of states at $(x/l_0 = 0)$ position. These lines represent levels that have a probability density at this position, as they are not affected by the presence of the barrier potential.

Figure 8 illustrates the effect of an external magnetic field and the Rashba spin-orbit coupling on the local density of states, where the figure displays the local density of states as a function of energy at $(x/l_0 = 1.7$) for a double quantum wire. Fig. 8(a) shows the local density of states in the absence of an external magnetic field. The first three vertical lines, each of them actually consists of four identical lines, meaning four degenerate energy levels, two because of the spin degenerate states and two due to the barrier. As for the remaining lines after the first three, each one represents two degenerate energy levels due to the spin because the barrier's effect vanished and did not work to merge the energy levels while Fig. 8(b) illustrates the local density of states under the presence of an external magnetic field ($\widetilde{\omega}_c = 1$). The effect of the external magnetic field becomes evident from this figure as it works to shift up energy levels, removes the spin degeneracy for all energy levels, and separates the merged energy levels caused by the barrier potential if they become higher than the barrier potential effective range. By raising the energy levels, the magnetic field effectively separates previously merged states that are pushed up higher than the barrier potential effective range. Consequently, states previously merged due to the barrier potential separate once more as evidenced by the four converging vertical lines in Fig. 8(b). The four converging vertical lines in the figure represent a single energy level before the magnetic field's influence, with the presence of the magnetic field, it separated into two levels, which were initially merged due

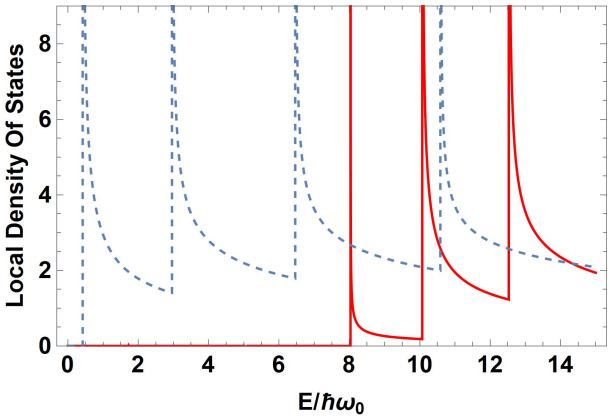

FIG. 7. Local density of states at $x/l_0 = 0$ for $\widetilde{\omega}_c = 0$, dashed lines for $\widetilde{\mu} = 0$, $\widetilde{\lambda} = 1$, solid lines for $\widetilde{\mu} = 2.5$, $\widetilde{\lambda} = 1$

to the barrier potential, and each level of these two levels split into two due to the removal of the spin degeneracy. The higher energy levels, which were not originally affected by the barrier potential, separate into two distinct levels upon the removal of spin degeneracy. The lower energy levels, such as the ground state, persist in their merged state due to the external magnetic field's insufficient strength to push it beyond the influence of the barrier potential, and the magnetic field only removed the spin degeneracy and separated it into two distinct levels. The Rashba spin-orbit coupling generates a significant separation in spin-up and spin-down states in the energy spectra levels. This is clearly evident when comparing Fig. 8(b), where ($\widetilde{\omega}_c$= 1) and ($\Delta_R/(\hbar\omega_0) = 0$), with Fig. 8(c), where ($\widetilde{\omega}_c$= 1) and ($\Delta_R/(\hbar\omega_0) = 0.1$). It is now evident how the Rashba spin-orbit coupling increases the separation between the spin-up and spin-down states.

Figure 9 illustrates the Local Density of States (LDOS) as a function of energy for the double quantum wire. Fig. 9(a) shows the LDOS at the position ($x/l_0 = 1.25$) corresponding to parameters $\widetilde{\mu}$= 2.5, $\widetilde{\lambda}$= 1, and in the absence of variation potential. Likewise, Fig. 9(b) exhibits the LDOS at position ($x/l_0 = -1.25$), maintaining the same parameter settings. A notable observation lies in the remarkable congruence between the LDOS profiles presented in Figs. 9(a) and 9(b) plots,

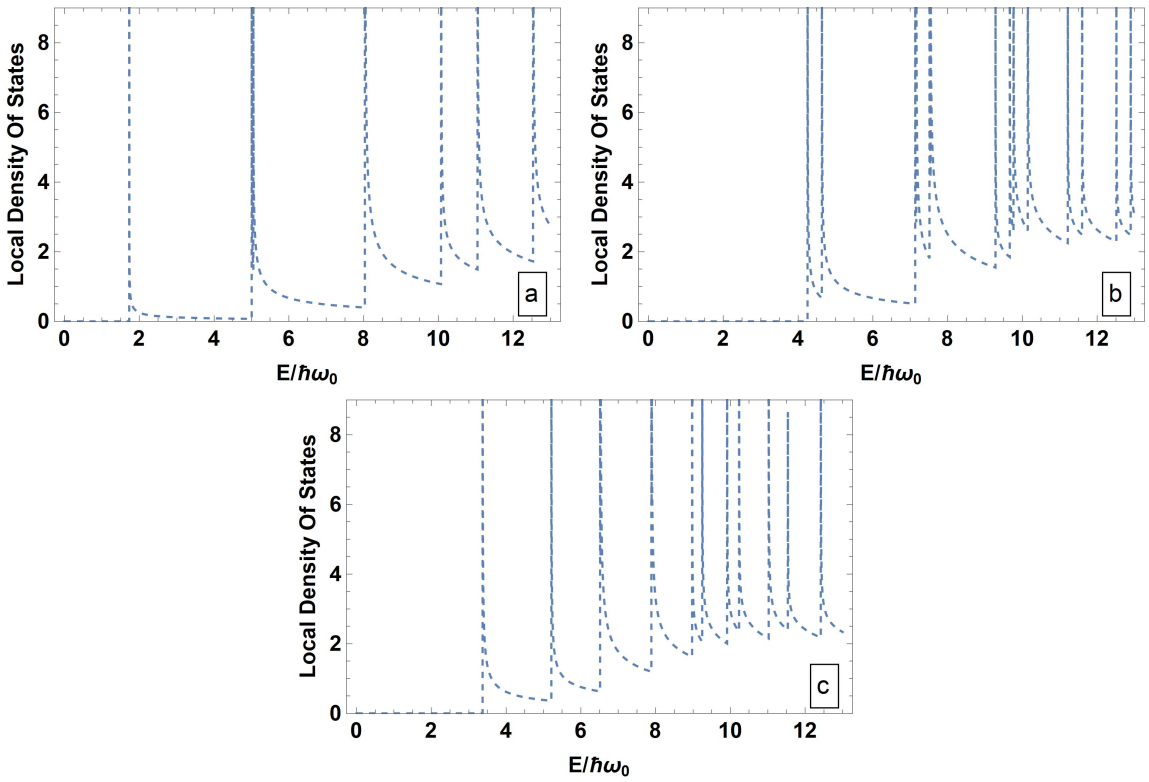

FIG. 8. Local density of states at $x/l_0 = 1.7$, $\widetilde{\mu}$= 2.5, $\widetilde{\lambda}$= 1; a) for $\widetilde{\omega}_c = 0$ and $\Delta_R/(\hbar\omega_0) = 0$; b) for $\widetilde{\omega}_c = 1$ and $\Delta_R/(\hbar\omega_0) = 0$; c) for $\widetilde{\omega}_c = 1$ and $\Delta_R/(\hbar\omega_0) = 0.1$

indicating a profound degeneracy in the energy levels between the two quantum wires. This observation supports the conclusions previously depicted in Fig. 2. Upon closer examination in Fig. 9(c) which represents the LODS for the same parameter settings in Fig. 9(a and b) but in the presence of variation potential ($V_0/(\hbar\omega_0) = 3$, $x_1/l_0 = 1.15$, $d/l_0 = 0.5$) where the dashed lines represent the LDOS plotted at the position ($x/l_0 = 1.25$) and the solid lines represent the LDOS plotted at the position ($x/l_0 = -1.25$). It becomes evident how the extra variation exerts a discernible influence on the energy spectra. Indeed, the introduction of the variation potential brings about a noticeable increase in the energy levels near its location (standard deviation of the Gaussian function chosen to be small (d/l_0= 0.5) to get more localized potential). This observation implies that the adding variation exerts a significant influence on the local electronic structure, resulting in changes to the energy levels within the quantum wire system. This observation aligns with the results discussed in Fig. 3. Furthermore, when examining the dashed and solid lines in Fig. 9(c), it becomes apparent that the two quantum wires exhibit different behaviors in respect to the variation potential. While one wire experiences notable shifts in its energy spectrum as a result of variation potential, the other wire remains relatively unaffected. This selective effect can be attributed to the deliberate choice of a Gaussian distribution, which confines the variation potential influence to specific regions within the quantum wire. Consequently, the difference in the energy profiles between the two wires confirms the localized nature of the variation potential distribution and their effect on the energy levels of the double quantum wire system.

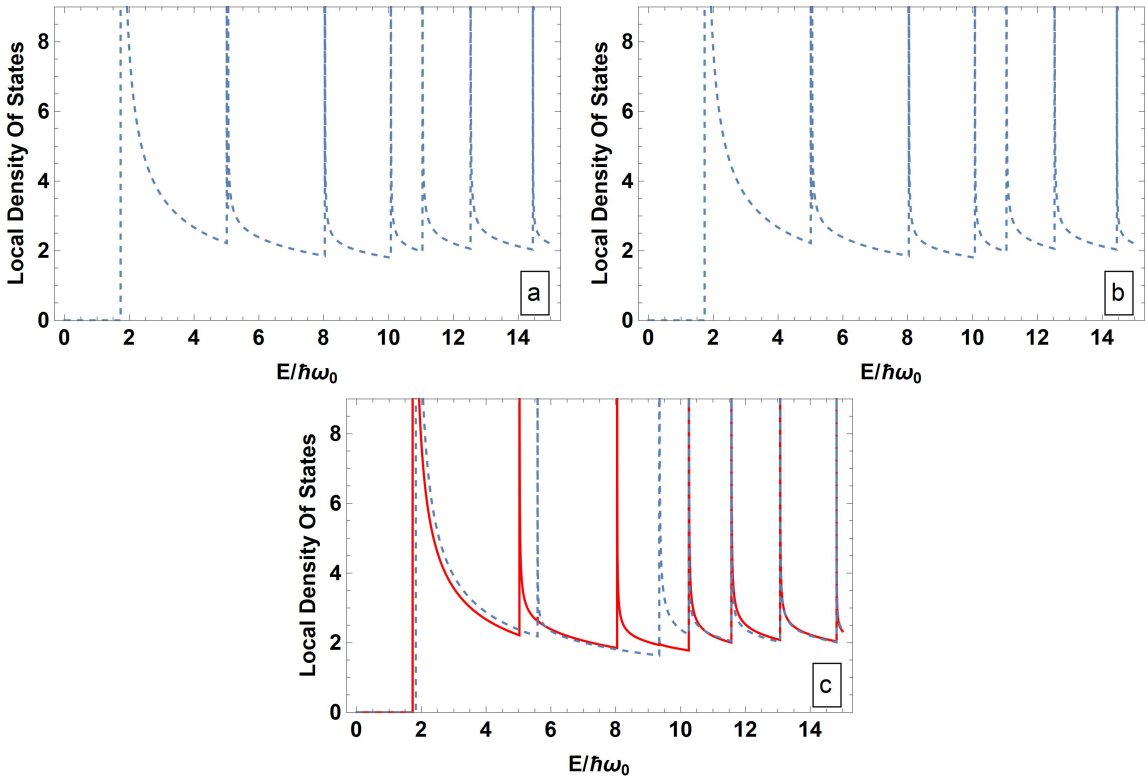

FIG. 9. Local density of states for $\widetilde{\mu} = 2.5$, $\widetilde{\lambda} = 1$ and $\widetilde{\omega}_c = 0$; a) $x/l_0 = 1.25$, without variation potential; b) $x/l_0 = -1.25$, without variation; c) dashed lines for $x/l_0 = 1.25$, $V_0/(\hbar\omega_0) = 3$, $x_1/l_0 = 1.15$, $d/l_0 = 0.5$, solid lines for $x/l_0 = -1.25$, $V_0/(\hbar\omega_0) = 3$, $x_1/l_0 = 1.15$, $d/l_0 = 0.5$

3. Conclusion

In conclusion, our study has provided a comprehensive understanding of the behaviors exhibited by double quantum wire (DQW) systems under varying structural parameters, variation potential, external magnetic field, and the Rashba spin-orbit coupling. Through detailed theoretical analyses and graphical representations, we have explained the effects of the confinement potential structural parameters μ and λ on the confinement potential profiles, probability density distributions, energy spectra, and local density of states in DQWs. Moreover, the introduction of variation potential within the DQW system has been discussed, makes significant alterations in the energy levels and the local density of states. Additionally, the influence of the external magnetic field and the Rashba spin-orbit coupling on the energy levels and the local density of states in the DQW system has been explored and discussed in detail. Overall, our findings contribute to advancing the understanding of quantum phenomena in DQW systems and offer valuable insights for the development of novel electronic devices and quantum technologies. Further experimental investigations are warranted to validate the theoretical predictions and explore practical applications of the observed phenomena in the real-world.

References

[1] Baghramyan H.M., Barseghyan M.G., Kirakosyan A.A., Restrepo R.L., Mora-Ramos M.E., Duque C.A. Donor impurity-related linear and nonlinear optical absorption coefficients in GaAs/$Ga_{1-x}Al_x$As concentric double quantum rings: Effects of geometry, hydrostatic pressure, and aluminum concentration. *J. of Luminescence*, 2014, **145**, P. 676-683.

[2] Dakhlaoui H. Linear and nonlinear optical absorption coefficients and refractive index changes in GaN/$Al_xGa_{(1-x)}$N double quantum wells operating at 1.55 μm. *J. of Applied Physics*, 2015, **117** (13), 135705.

[3] Kolokolov K.I., Beneslavski S.D., Minina N.Y., Savin A.M. Far-infrared intersubband absorption in p-type GaAs/Al_xGa_{1-x}As single heterojunctions under uniaxial compression. *Physical Review B*, 2001, **63** (19), 195308.

[4] Panda M., Das T., Panda B.K. Nonlinear optical properties in the laser-dressed two-level Al_xGa_{1-x}N/GaN single quantum well. *Int. J. of Modern Physics B*, 2018, **32** (4), 1850032.

[5] Liao Q.L., Jiang H., Zhang X.W., Qiu Q.F., Tang Y., Yang X.K., Liu Y.L., Huang W.H. A single nanowire sensor for intracellular glucose detection. *Nanoscale*, 2019, **11** (22), P. 10702–10708.

[6] Chen W., Cabarrocas P.R. Rational design of nanowire solar cells: from single nanowire to nanowire arrays. *Nanotechnology*, 2019, **30** (19), 194002.

[7] Robertson K.W., LaPierre R.R., Krich J.J. Efficient wave optics modeling of nanowire solar cells using rigorous coupled-wave analysis. *Optics Express*, 2019, **27** (4), A133–147.

[8] Espinet-Gonzalez P., Barrigón E., Otnes G., Vescovi G., Mann C., France R.M., Welch A.J., Hunt M.S., Walker D., Kelzenberg M.D., Åberg I. Radiation tolerant nanowire array solar cells. *ACS Nano*, 2019, **13** (11), P. 12860–12869.

[9] Hsu C.L., Wang Y.C., Chang S.P., Chang S.J. Ultraviolet/visible photodetectors based on p–n NiO/ZnO nanowires decorated with Pd nanoparticles. *ACS Applied Nano Materials*, 2019, **2** (10), P. 6343–6351.

[10] Chen Y., Hrachowina L., Barrigon E., Beech J.P., Alcer D., Lyttleton R., Jam R.J., Samuelson L., Linke H., Borgström M. Semiconductor nanowire array for transparent photovoltaic applications. *Applied Physics Letters*, 2021, **118** (19).

[11] Wu Y., Yang P. Direct observation of vapor- liquid- solid nanowire growth. *J. of the American Chemical Society*, 2001, **123** (13), P. 3165–3166.

[12] Pevzner A., Engel Y., Elnathan R., Ducobni T., Ben-Ishai M., Reddy K., Shpaisman N., Tsukernik A., Oksman M., Patolsky F. Knocking down highly-ordered large-scale nanowire arrays. *Nano letters*, 2010, **10** (4), P. 1202–1208.

[13] Madaria A.R., Yao M., Chi C., Huang N., Lin C., Li R., Povinelli M.L., Dapkus P.D., Zhou C. Toward optimized light utilization in nanowire arrays using scalable nanosphere lithography and selected area growth. *Nano Letters*, 2012, **12** (6), P. 2839–2845.

[14] No Y.S., Gao R., Mankin M.N., Day R.W., Park H.G., Lieber C.M. Encoding active device elements at nanowire tips. *Nano Letters*, 2016, **16** (7), P. 4713–4719.

[15] Chaure S., Chaure N.B., Pandey R.K. Self-assembled nanocrystalline CdSe thin films. *Physica E: Low-dimensional Systems and Nanostructures*, 2005, **28** (4), P. 439–446.

[16] Fischer S.F., Apetrii G., Kunze U., Schuh D., Abstreiter G. Tunnel-coupled one-dimensional electron systems with large subband separations. *Physical Review B*, 2006, **74** (11), 115324.

[17] Wang D.W., Mishchenko E.G., Demler E. Pseudospin ferromagnetism in double-quantum-wire systems. *Physical Review Letters*, 2005, **95** (8), 086802.

[18] Karaaslan Y., Gisi B., Sakiroglu S.E., Kasapoglu E.S., Sari H.Ü., Sokmen I. Rashba spin-orbit coupling effects on the optical properties of double quantum wire under magnetic field. *Superlattices and Microstructures*, 2016, **93**, P. 32–39.

[19] Gudmundsson V., Tang C.S. Magnetotransport in a double quantum wire: Modeling using a scattering formalism built on the Lippmann-Schwinger equation. *Physical Review B-Condensed Matter and Materials Physics*, 2006, **74** (12), 125302.

[20] Abdullah N.R., Tang C.S., Gudmundsson V. Time-dependent magnetotransport in an interacting double quantum wire with window coupling. *Physical Review B – Condensed Matter and Materials Physics*, 2010, **82** (19), 195325.

[21] Liu G., Liu R., Chen G., Zhang Z., Guo K., Lu L. Nonlinear optical rectification and electronic structure in asymmetric coupled quantum wires. *Results in Physics*, 2020, **17**, 103027.

[22] Su Y., Guo K., Liu G., Yang T., Yu Q., Hu M., Yang Y. Nonlinear optical properties of semiconductor double quantum wires coupled to a quantum-sized metal nanoparticle. *Optics Letters*, 2020, **45** (2), P. 379–382.

[23] Gisi B., Karaaslan Y., Sakiroglu S.E., Kasapoglu E.S., Sari H.Ü., Sokmen I. Effects of an in-plane magnetic field on the energy dispersion, spin texturing and conductance of double quantum wires. *Superlattices and Microstructures*, 2016, **91**, P. 391–400.

[24] Moon J.S., Blount M.A., Simmons J.A., Wendt J.R., Lyo S.K., Reno J.L. Magnetoresistance of one-dimensional subbands in tunnel-coupled double quantum wires. *Physical Review B*, 1999, **60** (16), 11530.

[25] Bielejec E., Reno J.L., Lyo S.K., Lilly M.P. Tunneling spectroscopy in vertically coupled quantum wires. *Solid State Communications*, 2008, **147** (3–4), P. 79–82.

[26] Huang D., Lyo S.K., Thomas K.J., Pepper M. Field-induced modulation of the conductance, thermoelectric power, and magnetization in ballistic coupled double quantum wires under a tilted magnetic field. *Physical Review B*, 2008, **77** (8), 085320.

[27] Karaaslan Y., Gisi B., Sakiroglu S.E., Kasapoglu E.S., Sari H.Ü., Sokmen I. Electric and magnetic field modulated energy dispersion, conductivity and optical response in double quantum wire with spin-orbit interactions. *Physics Letters A*, 2018, **382** (7), P. 507–515.

[28] Kumar S., Kumar M., Kumar A. Combined effect of rashba spin-orbit interaction, hydrostatic pressure and temperature on energy dispersion based ballistic conductance of InAs tunnel-coupled (double) quantum wire under exterior magnetic and electric field. *Physica B: Condensed Matter*, 2024, **677**, 415715.

[29] Korepov S.V., Liberman M.A. Tunnel-coupled double quantum wires in a magnetic field: electron scattering on impurities and boundary roughness. *Physica B: Condensed Matter*, 2002, **322** (1–2), P. 92–109.

[30] Sharma R. Impurity-modulated physical and transport properties in a In_xGa_{1-x}As double quantum wire. *Physica B: Condensed Matter*, 2023, **659**, 414845.

[31] Naydenov B., Boland J.J. Variable-height scanning tunneling spectroscopy for local density of states recovery based on the one-dimensional WKB approximation. *Physical Review B*, 2010, **82** (24), 245411.

[32] Widmer R., Gröning P., Feuerbacher M., Gröning O. Experimental signatures of spiky local density of states in quasicrystals. *Physical Review B*, 2009, **79** (10), 104202.

[33] Martín-Jiménez A., Fernández-Domínguez A.I., Lauwaet K., Granados D., Miranda R., García-Vidal F.J., Otero R. Unveiling the radiative local density of optical states of a plasmonic nanocavity by STM. *Nature Communications*, 2020, **11** (1), P. 1–8.

[34] Ivanov D.A., Ostrovsky P.M., Skvortsov M.A. Correlations of the local density of states in quasi-one-dimensional wires. *Physical Review B – Condensed Matter and Materials Physics*, 2009, **79** (20), 205108.

[35] Ignatchenko V.A., Tsikalov D.S. Local density of states in one-dimensional photonic crystals and sinusoidal superlattices. *Physics Procedia*, 2017, **86**, P. 113–116.
[36] Segovia-Chaves F., Vinck-Posada H., Navarro-Barón E.P. Local density of states in a one-dimensional photonic crystal with a semiconducting cavity. *Results in Physics*, 2022, **33**, 105129.
[37] Bena C., Kivelson S.A. Quasiparticle scattering and local density of states in graphite. *Physical Review B*, 2005, **72** (12), 125432.
[38] Shimomura Y., Takane Y., Wakabayashi K. Electronic states and local density of states in graphene with a corner edge structure. *J. of the Physical Society of Japan*, 2011, **80** (5), 054710.
[39] Karaaslan Y., Gisi B., Sakiroglu S., Kasapoglu E.S., Sari H.Ü., Sokmen I. Spin–orbit interaction and magnetic field effects on the energy dispersion of double quantum wire. *Superlattices and Microstructures*, 2015, **85**, P. 401–409.
[40] Hosseinpour P. Effect of Gaussian impurity parameters on the valence and conduction subbands and thermodynamic quantities in a doped quantum wire. *Solid State Communications*, 2020, **322**, 114061.
[41] Chen Q., Li L.L., Peeters F.M. Magnetic field dependence of electronic properties of MoS2 quantum dots with different edges. *Physical Review B*, 2018, **97** (8), 085437.
[42] Gradshteyn I.S., Ryzhik I.M., Romer R.H. *Tables of Integrals, Series, and Products*. American Association of Physics Teachers: College Park, MD, USA, 1988.
[43] Nilsson H.A., Samuelsson P., Caroff P., Xu H.Q. Supercurrent and multiple Andreev reflections in an InSb nanowire Josephson junction. *Nano Letters*, 2012, **12** (1), P. 228–233.

Submitted 11 September 2024; revised 5 October 2024; accepted 8 October 2024

Information about the authors:

Mahmoud Ali – Physics Department, An-Najah National University, Palestine; ORCID 0000-0002-3738-5851; mahmoud.Ali@najah.edu

Mohammad Elsaid – Physics Department, An-Najah National University, Palestine; ORCID 0000-0002-1392-3192; mkelsaid@najah.edu

Conflict of interest: the authors declare no conflict of interest.